Research Square

Preprints are preliminary reports that have not undergone peer review.
They should not be considered conclusive, used to inform clinical practice,
or referenced by the media as validated information.

Entropic Controlled Reduction of the three-body problem: regular islands, the chaotic transient and a Boltzmann solution at the gate

Daniele Schiano

schianodaniele1212@gmail.com

Universitas Mercatorum

Research Article

Keywords:

Posted Date: November 25th, 2026

DOI: https://doi.org/10.21203/rs.3.rs-11661097/v1

License: This work is licensed under a Creative Commons Attribution 4.0 International License.
Read Full License

Additional Declarations: No competing interests reported.

Entropic Controlled Reduction of the three-body problem: regular islands, the chaotic transient and a Boltzmann solution at the gate

Daniele Schiano

Universitas Mercatorum, Rome, Italy

schianodaniele1212@gmail.com

Abstract

We study the gravitational three-body problem using the Kolmogorov–Sinai entropy rate h_{KS} as a classifier of dynamical states (Entropic Controlled Reduction). Bounded orbits with $h_{\mathrm{KS}} = 0$ contain the stable Lagrange configurations, the stable choreographies and the stable hierarchical triples. For the figure-eight, Floquet analysis shows that stability is carried by the time modulation of the gravitational gain: the time-averaged gain is violently unstable, the modulated gain gives all multipliers on the unit circle, and the lateral torsion determinant is negative with certified sign. Outside this set the triple performs a chaotic transient on a saddle with two unstable directions, which ends because the pair potential has no floor. We then build the outcome distribution in the spirit of Boltzmann: the Liouville flux through a sphere in Jacobi coordinates, conditioned on a chaotic past and a confirmed escape, gives which body escapes and the energy and eccentricity of the final binary without free parameters. For unequal masses it reproduces simulations in two and three dimensions, whereas the Stone–Leigh ergodic theory overestimates the mass exponent of the escape probability (5.1–5.3 against 3.2–3.7). Time-resolved entropy shows that chaos is concentrated in democratic encounters, that long hierarchical phases are regular, and that the regular domain coincides with the Mardling–Aarseth boundary modified by inclination and Kozai–Lidov cycles.

1 Introduction

The general three-body problem has no analytic solution that maps initial conditions to outcomes [1, 2]. Two kinds of order nevertheless exist in it. The first is dynamical: periodic and quasi-periodic solutions, from the Lagrange triangle [22] to the figure-eight choreography [24, 25], around which motion is regular. The second is statistical: a bound, non-hierarchical triple almost always ends as a binary plus an escaping body [3–5], and the probabilities of the outcomes depend only on the conserved quantities and the masses [6–16].

Poincaré's question, where the bodies are at time t, has no closed answer for chaotic orbits. Boltzmann's question, what the probability of a state is, does. This paper treats both kinds of order with one tool: the Kolmogorov–Sinai entropy rate h_{KS} [17, 18]. We call the approach Entropic Controlled Reduction (ECR). h_{KS} is used in three ways: to classify initial conditions (the set $\mathcal{M}_{\mathrm{ECR}}$ of bounded orbits with $h_{\mathrm{KS}} = 0$), to resolve a chaotic orbit into regular and chaotic phases, and to condition the statistical measure on a chaotic history.

What Entropic Controlled Reduction is. The Kolmogorov–Sinai entropy rate measures how fast a dynamical system produces information about its initial condition. For a smooth Hamiltonian flow it equals the sum of the positive Lyapunov exponents (Pesin's formula [18]); on an open chaotic saddle it is reduced by the escape rate, $h_{\mathrm{KS}} = \sum \lambda^{+} - \gamma$ [31]. $h_{\mathrm{KS}} = 0$ means that nothing is forgotten: the motion is periodic, quasi-periodic on an invariant torus, or has left the region of interaction. $h_{\mathrm{KS}} > 0$ means that the state is being scrambled and only a statistical description is meaningful.

Entropic Controlled Reduction (ECR) is the programme of using h_{KS} as the organising quantity of a gravitational problem, instead of the individual trajectory. It rests on three operations. The first is a *reduction*: the phase space is partitioned into the set $\mathcal{M}_{\mathrm{ECR}}$ of bounded orbits with $h_{\mathrm{KS}} = 0$, where a deterministic description is available (periodic orbits, tori, stable hierarchies), and its complement, where only probabilities make sense. The second is a *time resolution*: along a single chaotic orbit, h_{KS} is measured phase by phase, which identifies when the system is being mixed and when it is moving regularly. The third is a *conditioning*: statistical predictions are weighted by the dynamical history that the entropy identifies, in particular by whether a state comes from a chaotic, democratic configuration.

The reduction is *controlled* in two senses. Passively, the dynamics itself selects the sets with $h_{\mathrm{KS}} = 0$: a stable periodic orbit keeps nearby motion regular, and an escape removes a body and ends the production of entropy. Actively, a feedback law can hold a system near a reference orbit of $\mathcal{M}_{\mathrm{ECR}}$; the linearised error

dynamics is then the damped counterpart of the equation that describes passive stability (Sec. 3). ECR does not claim that chaos always disappears: whether $h_{\rm KS}$ goes to zero depends on whether the system can escape, which in the gravitational problem is guaranteed by the absence of a floor in the pair potential (Sec. 5). In this sense ECR is a classification and a method, not a new law of motion, and every quantity it uses is measurable.

The paper is organised as follows. Section 2 fixes notation and numerics. Section 3 analyses the regular islands: the Lagrange configurations, the figure-eight and its mechanism of stability, and the active stabilisation of an unstable configuration. Section 4 describes the chaotic transient and Section 5 explains why it ends. Section 6 develops the Boltzmann description, from a master equation in shape space to the gate closure, which Sections 7–9 test against direct integrations and against the Stone–Leigh theory. Sections 10–11 resolve $h_{\rm KS}$ in time and map the regular hierarchical domain. Section 12 discusses scope, limitations and open problems.

2 Setup and numerical methods

Periodic orbits and their invariant tori are computed with the high-order methods described in Sec. 3. The statistical and entropy results use the integrator described here.

We use units with $G = 1$ and fix the total energy at $E = -0.5$; by the scaling symmetry of the Newtonian problem ($r \to \lambda r$, $t \to \lambda^{3/2} t$, $E \to E/\lambda$) results at other negative energies follow from the dimensionless angular momentum $L^2|E|$. The reference mass set is $m = (1, 0.6, 0.3)$; equal masses are used as a control. Orbits are integrated with a fourth-order Runge–Kutta scheme with step $\Delta t = \eta\, r_{\rm min}^{3/2}$, $\eta = 0.004$, capped at 0.02, where $r_{\rm min}$ is the smallest pairwise distance. Orbits whose relative energy error exceeds 10^{-5} are discarded; this removes about 0.5% of the sample. Halving the step leaves all reported statistics unchanged within errors.

Escape. Body k is declared escaping when its distance from the centre of mass of the other two exceeds 20, its two-body energy relative to that pair is positive, and it is moving outwards. We require in addition that the remaining pair be bound with $x \equiv E_B/E > 1$, so that the escaper has positive energy at infinity. The condition excludes wide triples whose pair is as large as the detection radius. Such configurations amount to 8.5%, 5.5% and 1.6% of the candidate escapes of the heavy, middle and light body in the planar sample; counting them as escapes would bias α downwards by 0.3–0.5, increasingly with age.

Phases. At each time the configuration is labelled *democratic* when no pair is hierarchically separated from the third body, *calm* when one pair is bound and the third body is outside three times the pair's semi-major axis, *intermediate* in between, and *unbound* when the third body has positive energy relative to the pair. A purely distance-based criterion (all pairwise distances below a threshold) is not adequate, because it classifies compact hierarchical triples as democratic; the hierarchy-based definition is used throughout.

Entropy. We integrate the variational equations together with the orbit and renormalise the tangent vectors every 8 time units. The tangent space is reduced by projecting out the centre-of-mass motion, rigid rotations, the scaling direction and the flow direction, and lengths are measured in the mass metric; what remains is deformation of the shape on the energy shell. With two tangent vectors the sum of the two positive exponents gives $h_{\rm KS}$ by Pesin's formula [18]. Shadow-orbit estimates with a finite perturbation (10^{-8}) are affected by numerical noise in calm phases, where they exceed the tangent result by about 30%; on test orbits the tangent method agrees with a calibrated shadow estimate (0.0182 against 0.0179). A segment is classified as regular when its accumulated tangent growth increases at most logarithmically with its duration.

3 Regular islands

We define $\mathcal{M}_{\rm ECR}$ as the set of initial conditions whose forward orbit remains bounded and has $h_{\rm KS} = 0$. Boundedness is part of the definition: an escaped final state also has $h_{\rm KS} = 0$, but it is the endpoint of the transient, not an island. Within $\mathcal{M}_{\rm ECR}$ we find two types of regular islands [26]. *Kolmogorov* islands surround elliptic equilibria in a rotating frame (Lagrange); *Rüssmann* islands surround stable periodic orbits whose twist degenerates in one direction (the choreographies).

3.1 Lagrange configurations

The equilateral configuration of three masses is a relative equilibrium for any masses. Its linear stability is decided by Routh's criterion [22]: the configuration is linearly stable if and only if

$$27\,(m_1m_2 + m_2m_3 + m_3m_1) < (m_1 + m_2 + m_3)^2, \quad (1)$$

which in the restricted problem reduces to Gascheau's threshold $\mu < \mu_c = 0.03852$. Equal masses violate Eq. (1): the equal-mass Lagrange configuration is unstable, with a real part of the leading eigenvalue 0.63 in the rotating frame. For the Sun–Earth ($\mu \simeq 3 \times 10^{-6}$), Sun–Jupiter ($9.5 \times 10^{-4}$) and Earth–Moon (0.0121) systems the variational eigenvalues at L_4 are purely imaginary (real parts at the level of 10^{-16}), with two libration frequencies, and $h_{\rm KS} = 0$: these are Kolmogorov islands.

At equal masses the Hessian of the potential on the shape space, after removal of translations and rotations, has eigenvalues 9.000, 4.500, 4.500: a degenerate pair (the shape modes) and an isolated breathing mode, the structure required by Schur's lemma for the symmetric configuration. The cubic term of the expansion gives an isotropic torsion $d\omega/dI = -2025\, I/(16384\,\omega_0^4)$. For unequal masses the degenerate pair splits. We computed

the Birkhoff torsion at L_4 in the restricted problem with a pipeline that reproduces the zero of the torsion found by Deprit and Deprit-Bartholomé [23] at $\mu = 0.01093$, against the exact 0.0109137 (error 0.15%); we use this, together with the Sitnikov problem [27], as a validation benchmark. The vanishing of the Lagrange torsion at isolated mass ratios is an accidental degeneracy, structurally different from the symmetry-imposed degeneracy of the figure-eight discussed next.

The mass ratio therefore selects the stability mechanism available: a dominant mass allows Lagrange libration; equal masses exclude it, and the regular islands at equal masses are the choreographies.

3.2 The figure-eight: numerics

The figure-eight [24] was computed with a Taylor integrator of order 16–20 in multiple precision and refined by Newton iteration to a closure residual at machine zero at 40 digits; a Krawczyk enclosure certifies the initial condition in the three parameters left after fixing the rotational gauge. The reference orbit has period $T = 6.325914$ at energy $E = -1.287142$. Its KAM stability has a computer-assisted proof [25]; the analysis below concerns the mechanism, not a new proof.

The complex-time singularities of the orbit, located by rational (AAA) approximation, lie at the midpoints between collinear configurations, at $\operatorname{Im} t^* \approx 0.52$, with spacing $T/6$: the six collinear passages per period fix the period of the singularity lattice, in agreement with the D_6 symmetry of the orbit.

3.3 Stability by modulation

Linearising the equations of motion around the orbit, the perturbation obeys $\ddot{\boldsymbol{\xi}} = J(t)\,\boldsymbol{\xi}$, where $J(t) = \partial\mathbf{F}/\partial\mathbf{q}$ is the gravitational gain evaluated along the orbit; it is periodic and varies strongly (relative variability 3.5 over a period). We compare two monodromy matrices over one period. With the true, modulated gain, all twelve Floquet multipliers lie on the unit circle, $|\mu|_{\max} = 1.0000$. With the gain frozen at its time average, $|\mu|_{\max} \approx 2.3 \times 10^3$: the averaged gravity would make the orbit violently unstable, and its eigenvalues are all non-negative. The stability lives in the modulation, not in the mean.

The power spectrum of $|J(t)|$ is dominated by the sixth harmonic of the period (power 1807, against 132 at the twelfth and negligible elsewhere): the gain is modulated once per collinear passage. Rescaling the modulation frequency, $J(t) \to J(\omega t/\omega_0)$, the largest multiplier develops a deep and narrow minimum at the true frequency (Fig. 1, right): $|\mu|_{\max} = 9112$, 1143, 135, 26 at $\omega/\omega_0 = 0.85$, 0.90, 0.95, 0.98; 1.0003 and 1.0000 at 1.00 and 1.02; 11, 35, 55 at 1.05, 1.10, 1.15. The band is a few percent wide and asymmetric, much steeper on the low-frequency side, and the orbit sits just below its centre.

Mathieu reduction. Reducing the 12×12 problem to one degree of freedom,

$$\ddot{x} + 2d\,\dot{x} + \big[p + 2q_{\mathrm{amp}}\cos(2\omega t)\big]x = 0, \qquad (2)$$

with p the mean curvature, q_{amp} the modulation amplitude and d a damping, the figure-eight has $(p, q_{\mathrm{amp}}) \simeq (0, 0.21)$, $d = 0$. Fig. 1 (left) shows the Ince–Strutt stability chart of Eq. (2) at $d = 0$, $\omega = 1$. The figure-eight lies in the stable region ($|\mu|_{\max} = 1.000000$) close to its lower boundary $a_0(q) \simeq -q^2/2 = -0.022$; the equal-mass Lagrange point, $(0, 1.11)$, has $|\mu|_{\max} = 3.65$, and the Euler collinear configuration, $(-1.33, 0)$, has $|\mu|_{\max} = 37.5$, both unstable as known. The region $a_0(q) < p < b_1(q)$ with $p < 0$ is the Kapitza-type region, in which a mode that is unstable on average is stabilised by modulation; the inverted pendulum with a vibrating pivot is its small-q limit. The reduction to two scalars is approximate, and the position close to the boundary means that p must be quoted with its uncertainty: at $q_{\mathrm{amp}} = 0.21$, $p = -0.02$ is still stable while $p = -0.03$ gives $|\mu|_{\max} = 1.33$.

Role of the symmetry. For the figure-eight, the choreographic $\mathbb{Z}_3$ symmetry with six collinear passages per period produces a modulation dominated by the sixth harmonic, and that frequency falls in the stable band. This is the mechanism of this orbit, not a general implication: most three-body choreographies found numerically are unstable [28], although they share the $\mathbb{Z}_3$ symmetry, and the number of collinear passages depends on the shape of the orbit.

Scaling. By the homogeneity of the Newtonian potential, the modulation frequency obeys $\omega(E) = C\,|E|^{3/2}$ exactly for $E < 0$, with $C = 4.081014577$ for the sixth harmonic of the figure-eight, and $C = 2\sqrt{2}/3$ for the rotation of the equal-mass Lagrange configuration. The figure-eight therefore remains at the same point of its stability band at every negative energy: its stability is a property of the shape of the orbit, not of its energy. At $E = 0$ the modulation frequency vanishes.

3.4 Torsion: lateral and longitudinal

The degenerate twist of the figure-eight noticed in the Birkhoff normal form concerns the longitudinal direction, along the orbit, where the stabilisation is parametric. In the two lateral directions the torsion is non-degenerate. Invariant 2-tori with lateral rotation frequencies $\omega = 2.7187$ and 2.0768 were computed by Fourier–Newton continuation, with symplectic normalisation of the modes. Interval arithmetic (CAPD) gives $T_{11} \in [-5.84, -5.44]$ and $T_{22} \in [35.08, 35.37]$; since $T_{11}T_{22} < 0$, the determinant $T_{11}T_{22} - T_{12}^2$ is negative for any T_{12}. In floating point with symplectic normalisation the full matrix is symmetric to 10^{-4}, with $T_{12} = -4.585$ and $\det T = -26.2$ (different normalisation, same signs). The tori are approximate, with invariance residuals of 1–4 $\times\, 10^{-3}$ under the rigorous flow; the certified statement is the sign of the determinant on these approximate tori, which is the Rüssmann

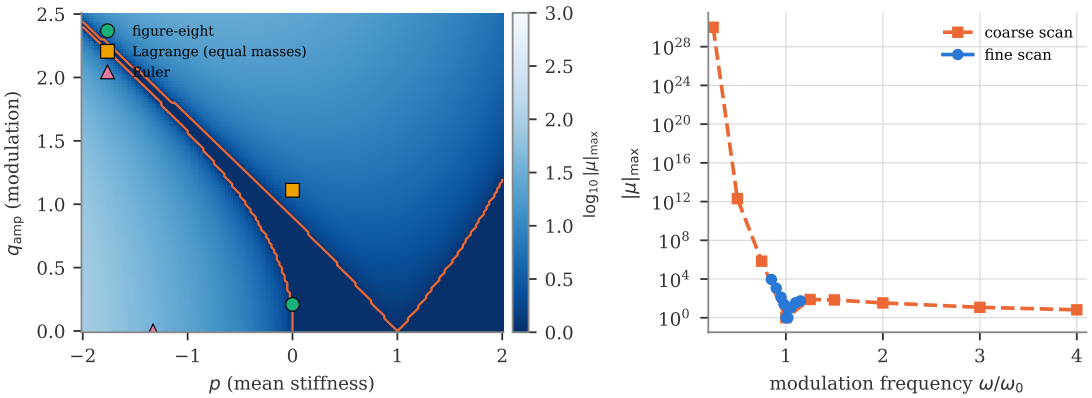

Figure 1: Left: Ince–Strutt stability chart of the Mathieu equation (2) at $d = 0$, colour $\log_{10}|\mu|_{\max}$ (dark = stable, contour $|\mu|_{\max} = 1$), with the measured positions of the figure-eight, the equal-mass Lagrange point and the Euler configuration. Right: largest Floquet multiplier of the figure-eight when the modulation frequency of the gravitational gain is rescaled; the true frequency is $\omega/\omega_0 = 1$.

non-degeneracy condition in the lateral directions. For the stable choreography NC1 of Šuvakov and Dmitrašinović [26] the same lateral sector gives $\det T < 0$ in 100% of bootstrap resamples; among five Šuvakov orbits examined, the two stable choreographies have invariant tori with $\det T < 0$ and the three unstable orbits have none.

3.5 Vertical stability

Out of the plane, the vertical perturbations decouple at first order by the symmetry $z \to -z$ and obey $\ddot{\mathbf{u}} = A(t)\mathbf{u}$ with A built from the planar distances. For the figure-eight all four vertical multipliers lie on the unit circle: the apparent excess over 1 halves at each doubling of the resolution and extrapolates to zero, consistent with Ref. [29]. For NC1, co-integrated with the orbit (closure residual 1.9×10^{-11}), all four multipliers have $|\mu| = 1.00000000$ in two pairs of complex-conjugate modes. The stability of both stable choreographies is genuinely three-dimensional.

3.6 Active stabilisation

The same linear structure describes an active control that holds a system near a reference orbit $\tilde{\mathbf{q}}(t)$ in $\mathcal{M}_{\mathrm{ECR}}$:

$$\dot{\mathbf{p}} = \mathbf{F}_{\mathrm{grav}} - 2\alpha(\mathbf{q} - \tilde{\mathbf{q}}) - 2\alpha\beta(\mathbf{p} - \tilde{\mathbf{p}}) - 2\alpha\gamma \int (\mathbf{q} - \tilde{\mathbf{q}})\, dt. \tag{3}$$

With constant gain and $\gamma = 0$ (proportional–derivative law) the error converges above the threshold $\beta_c = 1$, independent of α; the PD law leaves one neutral pole, which the integral term moves to -0.36 ($\gamma = 0.5$) and -0.72 ($\gamma = 1$). Below threshold, at $\beta = 0.5$, the integral term reduces the residual distance from 1.09 to 0.74. In terms of Eq. (2), the passive figure-eight and the active control are two regions of the same diagram: $d = 0$ with a tuned modulation (stability by resonance, the reference orbit is a neutral torus) and $d > 0$ with constant gain (stability by contraction, the reference orbit becomes an attractor). Liouville's theorem forbids attractors in the conservative problem, which is why the passive mechanism must be resonant. The active controller does not destroy the information produced by the chaotic dynamics; it absorbs it, at a thermodynamic cost of at least $k_B T \ln 2$ per erased bit.

4 The chaotic transient

Outside $\mathcal{M}_{\mathrm{ECR}}$ a bound triple wanders on a chaotic saddle until it disintegrates. We characterised the saddle at $E = -0.5$, $L = 0$, equal masses, on an ensemble of 1300 orbits, of which 99.3% decay within the integration time.

4.1 Lifetime

The lifetime distribution separates into a prompt part ($T < 10$) and a diffusive part ($T > 60$). An exponential fit to the diffusive tail gives $\tau = 133 \pm 6$ (bootstrap 95% interval $[121, 146]$). An independent estimate from a Markov model in the variables (θ, L, E_B), where θ is the polar angle on Montgomery's shape sphere measured from the Lagrange point [30], gives 144.7 ± 7.9, compatible. The smallest shape angle reached by an orbit correlates with its lifetime (Spearman $\rho = -0.670$).

4.2 Two unstable directions

The saddle has two positive Lyapunov exponents, $\lambda_1 = 0.0565$ and $\lambda_2 = 0.0175$, with converged estimates (tangent renormalisation step checked). The escape rate is $\gamma = 0.0073$ ($1/\gamma = 137$), and the Kantz–Grassberger relation [31] gives the entropy of the saddle, $h_{\mathrm{KS}} = \sum \lambda^+ - \gamma = 0.067$; the partial information dimension along the leading direction is $d_1 = 0.902$. The static counterpart of the two unstable directions is visible at the Euler configuration, where the Hessian of the potential has two negative eigenvalues, two zero modes (symmetries) and two positive ones. Measuring the vertical exponent on the saddle with the eigenvalues of the

4×4 vertical monodromy (singular-value and single-vector estimates are biased by the non-normality of elliptic modes) gives an apparent λ_z that decays with the integration horizon, from 0.030 to 0.018; it is bounded by the lifetime of the saddle orbits and provides only an upper limit, $\lambda_z \lesssim 0.018$. No third escape direction out of the plane is found.

4.3 Renewal structure

The diffusive orbits alternate democratic episodes with temporary hierarchical captures, identified by jumps of the binary energy; these captures account for 33% of the stickiness. With N the number of episodes (geometric, mean 3.12), a cycle duration of 24.4 and a capture duration of 28.8, the renewal estimate

$$\tau = (N-1)(t_{\rm cycle} + t_{\rm capt}) + t_{\rm cycle} = 137 \qquad (4)$$

reproduces the measured lifetime. A two-stage model (injection followed by renewal) gives a prompt fraction of 67.6% against 73% measured and a tail time of 145.5.

Lagrange as injector. Initial conditions biased towards the Lagrange configuration enter the diffusive regime in 64% of cases, against 2% for random initial conditions at the same angular momentum, a factor of about 30; they leave the Lagrange region within 25 time units along its unstable manifold. The rate of large jumps of θ decreases monotonically from 0.082 near Lagrange to 0.0022 at $\theta \simeq 0.54$. At equal masses the Lagrange region is the entrance to chaos, and the binary hierarchy is its exit.

4.4 Scale invariance and the Kantz–Grassberger relation

With escape thresholds rescaled with the energy ($s = 0.5/|E|$ for lengths, $s^{3/2}$ for times), 3000 orbits per energy at $E = -0.3, -0.5, -0.7$ give the values of Table 1. (Initial positions uniform in $[-1,1]^2$ with minimum separation 0.4; with this generator the lifetime at $E = -0.5$ is 156 ± 12 instead of 133 ± 6.) The rescaled rates $\gamma/|E|^{3/2}$ and $\lambda_i/|E|^{3/2}$ are constant within about 10%: once units are rescaled there is no residual energy dependence. The codimension of the saddle measured independently with the uncertainty exponent, $D - d = 0.198$ at $E = -0.5$, reproduces the value 0.200 obtained from the escape statistics. The Kantz–Grassberger time with a single codimension, $\tau_{\rm KG} = 1/[\sum \lambda^+ (D-d)]$, is shorter than the measured lifetime by a factor 2.4–3.1, constant in energy: the scaling is right and the prefactor is not. With two unstable directions the relation requires the partial dimensions along each, $\gamma = \lambda_1(1 - d^{(1)}) + \lambda_2(1 - d^{(2)})$, and the temporary hierarchical captures lengthen the tail further. With an energetic escape criterion (third body with positive energy, pair separated by less than a quarter of its distance) the tail time is 997 ± 70 at $E = -0.5$, and 72–80% of the tail time is spent in bound hierarchical captures.

Table 1: Scale invariance of the saddle with rescaled thresholds (geometric criterion, 3000 orbits per energy). $\tau_{\rm KG} = 1/[\sum \lambda^+ (D-d)]$.

	$E = -0.3$	$E = -0.5$	$E = -0.7$
$1/\gamma$	333	156 ± 12	104
$\gamma/\lvert E\rvert^{3/2}$	0.0183	0.0181	0.0164
$\lambda_1/\lvert E\rvert^{3/2}$	0.203	0.181	0.180
$\lambda_2/\lvert E\rvert^{3/2}$	0.112	0.099	0.090
$D - d$	0.141	0.198	0.174
$(1/\gamma)/\tau_{\rm KG}$	2.4	3.1	2.9
time in captures	0.10	0.21	0.12

4.5 Persistence is a transport property

The probability that a temporary capture persists, $p \approx 0.37$, is not predicted by any local variable: the energy, radial velocity and angular momentum of the third body, the semi-major axis of the pair, the distance ratio, the phase and the instantaneous Lyapunov exponent all fail to separate persistent from non-persistent captures, and so does the coherence of Kozai–Lidov oscillations in fully three-dimensional integrations (coherence 0.020 against 0.026 in the control group: the inclination is agitated chaotically in both, because these captures are not hierarchies with a clean separation of scales). The local disruption theories of Monaghan and Heggie, based on the energy of the escaper, do not apply in this regime. The codimension of the basin boundary deviates from the value expected from the entropy balance of Ref. [32]: $D - d = 0.200$ [0.167, 0.257] against 0.099 at $E = -0.5$. Both facts indicate that p is a property of transport on the saddle, governed by its stable and unstable manifolds (lobe dynamics), and not of the local state. The Sitnikov problem, in which the lobe machinery reproduces Moser's picture [27] (regular motion at zero eccentricity, a fractal separatrix and compact KAM islands at $e = 0.3$), was used to validate the transport computations.

5 Why chaos ends: the bottomless well

The decay of $h_{\rm KS}$ along gravitational three-body orbits is not a general property of Hamiltonian chaos. In closed systems it does not happen: in a confined box, in the heavy top, in the Lorenz flow and in the Hénon–Heiles potential the entropy rate stays positive indefinitely. In the three-body problem it happens because the pairwise potential has no floor. A bound pair can absorb arbitrarily large negative energy, which pays for the escape of the third body, and the Boltzmann entropy of the system has no maximum.

We verified this by softening the pair potential to $-m_i m_j/\sqrt{r^2 + \varepsilon^2}$. The fraction of orbits that escape within the integration time drops from about 80% to zero exactly at the value of ε at which the softened well's floor rises above the total energy, here $\varepsilon = 2$. Above that threshold escape is energetically forbidden, and 136 of 140 orbits remain chaotic for the whole inte-

gration; the other four are regular from the start. The same threshold, predicted from the energy alone, holds for unequal masses and for four bodies. Escape is the mechanism by which $h_{\rm KS}$ goes to zero, and the statistical theory of the next section is a theory of how the system crosses that threshold.

6 From Poincaré to Boltzmann

Poincaré's obstruction concerns the trajectory $\mathbf{r}_i(t)$. A Boltzmann description asks instead for the evolution of a probability density over states, and for the distribution of outcomes. For the three-body problem this replaces an impossible deterministic map by a question that can be answered. This section describes the route from a kinetic equation in shape space to a closure at the gate, and the role played along the way by the collision wall and by Sundman's regularisation.

6.1 A master equation on the shape sphere

The natural kinetic variable is the polar angle θ on the shape sphere, measured from the Lagrange point, with the exact pair distances $r_{ab}^2 \propto 1 - \sin\theta\cos(\phi - 2\pi(a-1)/3)$ [30]. Near Lagrange the motion in θ is not overdamped: regressing $\ddot\theta$ on $\dot\theta$ and on the azimuthal rotation $\dot\psi^2$ around the Lagrange point shows a centrifugal term $\theta\dot\psi^2$ whose fitted coefficient equals θ itself (ratio 0.9–1.0 in most bins). With the exact centrifugal term and the harmonic potential, without any friction term, the equation explains 76% of the variance of $\ddot\theta$ ($R^2 = 0.760$). Neither a viscous term in $\dot\theta$ nor an anharmonic term in θ^3 explains the remainder ($R^2 < 0.06$).

The remainder is a jump process. The increments of θ have excess kurtosis 5.96, and the top 1% of jumps carries 21% of the variance. Large jumps inject energy rather than dissipating it: in 76% of them the kinetic energy of θ increases, by 141% on average. They are close encounters. Their rate decreases from 0.082 near Lagrange to 0.0022 at $\theta = 0.54$, a factor 38, while their size changes by a factor 1.6 only. The diffusion coefficient measured by Kramers–Moyal is accordingly the sum of a jump part and a regular part,

$$D(\theta) = 0.034\, e^{-\theta/0.178} + (0.0223 - 0.0209\,\theta), \qquad (5)$$

which reproduces the measured $D(\theta)$ with $R^2 = 0.986$. The decay length of the jump part is not free: fitting rate and squared size separately gives decay lengths 0.2155 and 1.0624, and $1/0.2155 + 1/1.0624 = 5.58$ against $1/0.178 = 5.63$. Far from Lagrange the transport is diffusive (mean-square displacement $\propto t^{1.014}$). The resulting master equation has three regimes: near Lagrange ($\theta < 0.15$) a linear instability with rate 0.236 and concentrated jumps; a transition region ($0.15 < \theta < 0.40$); and an ordinary Fokker–Planck regime with absorbing boundary at large θ, where the saddle entropy $h_{\rm KS} = 0.067$ and the lifetime $\tau = 133$ apply.

This description is correct as kinetics but does not close for escape. Conditioned on θ, the probability of escape is not determined: θ is not a Markovian variable for the outcome, because the same shape is visited both by systems that will escape and by systems that will return. A closure requires a variable in which the outcome is decided.

6.2 The collision wall

Close approaches are where the jumps happen, and it is natural to ask whether the proximity to collision, the "wall" at $r_{\rm min} \to 0$, carries the information that θ lacks. Three tests say it does not. The complex-time singularities of chaotic orbits, located by the same AAA method that reproduces the figure-eight singularities at $\mathrm{Im}\, t^* \approx 0.52$, show no reproducible dependence on the depth of the approach ($n = 18$ and 68 orbits, sign of the correlation unstable between samples), although the same idea works in the Sitnikov problem, where $\mathrm{Im}\, t^*$ halves as the eccentricity grows. At fixed $r_{\rm min}$ compact and wide initial conditions remain distinguishable (Sec. 8); and the excess eccentricity of binaries whose pair touched the wall is a kinematic consequence of a small pericentre, not a cause. The wall organises where jumps occur, not where the system goes.

6.3 The gate

The variable in which the outcome is decided is the energy of the third body at a sphere $r_3 = R$ around the pair. At the gate the sign of E_3 decides deterministically whether the body escapes or returns, and returning bodies follow Keplerian flight times. The question then becomes the measure of states at the gate. Three ingredients are necessary.

Time reversal. The flux measure at the gate is symmetric under time reversal and therefore contains scattering states, in which the third body arrives from infinity: 29.8% of the theoretical gate states, against 1.7% in the simulated orbits. Excluding them by integrating each state backwards is the step that makes the measure predictive.

Sundman time. Sampling the gate in Sundman's regularised time instead of physical time introduces a weight that grows with the proximity to collision (a monotonic relation in all six configurations of the angular-momentum family, significance $p = 0.045$ before correction for multiple tests). The pure Liouville measure in physical time, with the backward filter, needs no such weight and is the one used below.

Keplerian excursions. The returns through the gate are Keplerian excursions. Near the escape threshold the density of outer energies is finite, so with $|E_3| \to 0$ the excursion period $\propto |E_3|^{-3/2}$ gives $P(T > t) \propto t^{-2/3}$, a density $\propto t^{-5/3}$ with an amplitude fixed by the gate measure. The measured tail of the lifetime distribution of escaped systems has exponent 1.70 [1.63, 1.76] between 300 and 3000 and 1.67 [1.53, 1.81] up to 3×10^4 (Sec. 10), in agreement with 5/3. The process is thus a renewal process at the gate with exactly treated excursions, the structure of the random-walk model of Ginat and Perets [15] and of the Lévy-flight description of Manwadkar, Trani and Leigh [16].

With these ingredients the gate measure, conditioned on the past, reproduces the outcome distribution of two independent held-out samples without free parameters (Kolmogorov–Smirnov distance 0.007 on both), with identical results on two machines. Across twelve physically distinct configurations (gate position $R|E|$, angular momentum $L^2|E|$, mass ratios), conditioning on a single bound episode passes a strict survival-tail test in 5 configurations, while conditioning on the confirmed arrival age of the state passes in 11. The remaining difference between a bound past and a chaotic past is the subject of the next section.

7 The gate measure

Let $\mathbf{r}$ be the Jacobi vector of a candidate binary (i, j) and $\boldsymbol{\rho}$ that of the third body k relative to the binary's centre of mass, with reduced masses $\mu_B = m_i m_j/(m_i + m_j)$ and $\mu_k = m_k(m_i + m_j)/M$. Jacobi coordinates are canonical, so the Liouville measure has the same form in all three channels. The gate is the sphere $|\boldsymbol{\rho}| = R$. The microcanonical flux through it is

$$d\Phi_k = \delta(H - E)\,\delta(\mathbf{L} - \mathbf{L}_0)\,\frac{p_\rho}{\mu_k}\,\Theta(p_\rho)\,d^d r\,d^d p\,dS_\rho\,d^d p_\rho, \tag{6}$$

restricted to states in which the pair is bound with $x > 1$ and $|\mathbf{r}| < R/2.5$. Integrating the energy delta over $|p_\rho|$ leaves a weight $\mu_k|p_\rho|$; we sample the remaining variables uniformly and weight each state accordingly.

Eq. (6) alone is the ergodic flux. Two dynamical conditions select the states that are actual outcomes of chaotic evolution:

1. *Chaotic past.* Integrated backwards in time, the state reaches a democratic configuration before escaping to infinity. A state whose past is a body arriving from infinity is a scattering state and is not an outcome of a bound triple.

2. *Confirmed escape.* Integrated forwards, body k reaches the detection radius with positive energy without returning to a democratic configuration.

Condition 1 is the ECR ingredient. Requiring only a bound past is not sufficient: with that weaker condition the agreement with simulations degrades with the age of the system (χ^2 rising from 6.8 to 17.9), while with the chaotic past it does not. By time-reversal symmetry, the fraction of gate states that satisfy condition 1 is Kol's chaotic absorptivity [12], here computed state by state instead of being measured from independent scattering runs.

To compare with a population of systems of age $\geq a$, condition 1 is imposed with a backward horizon equal to a. Prompt escapes, which retain memory of how the initial conditions were drawn, are obtained by weighting the same gate states with the density of the initial-condition generator; the split between prompt and relaxed escapes then follows from the integration and is not fitted. For each of the three initial-condition generators of Sec. 8, this weighting reproduces the prompt part of the escape statistics.

Table 2: Planar mass exponent α, simulations against the gate theory with chaotic past ($R = 6$, masses 1:0.6:0.3, $E = -0.5$).

	age ≥ 100		age ≥ 150	
$L^2\|E\|$	sim	gate	sim	gate
0–0.01	3.17 ± 0.14	3.00	3.30 ± 0.19	2.98
0.01–0.03	3.08 ± 0.16	2.88	2.88 ± 0.17	2.85
0.03–0.06	2.76 ± 0.13	2.85	2.70 ± 0.16	2.86
0.06–0.12	2.26 ± 0.09	2.28	2.26 ± 0.10	2.27
0.12–0.25	2.20 ± 0.07	2.27	2.24 ± 0.10	2.24
0.25–0.50	2.75 ± 0.14	2.86	2.72 ± 0.16	2.81
χ^2 (6 bins)	2.2		1.7	

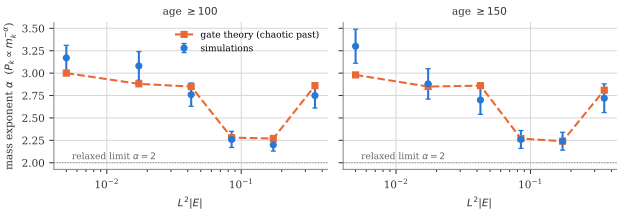

Figure 2: Planar mass exponent against angular momentum. Circles: direct integrations with statistical errors; squares: gate theory with chaotic past ($R = 6$). The dotted line is the relaxed phase-space value $\alpha = 2$.

In the relaxed limit the unconditioned gate measure reduces to the classical phase-space counting: the escape probability scales as m_k^{-2} in the plane and m_k^{-3} in three dimensions [10], and the binary eccentricity distribution is thermal ($2e$ in 3D). The conditioning modifies these laws at finite angular momentum, which is where the tests below are discriminating.

8 Planar tests

Figure 2 and Table 2 compare the mass exponent α, obtained from a power-law fit $P_k \propto m_k^{-\alpha}$ to the three channels, with the gate prediction for a gate radius $R = 6$. The exponent depends strongly on angular momentum, from $\alpha \approx 3.2$ at $L \approx 0$ to 2.2 at intermediate L and back to 2.75 at high L. The gate theory follows this non-monotonic curve without adjustment: $\chi^2 = 2.9$, 2.2 and 1.7 over six bins for ages ≥ 50, 100 and 150. The escape criterion of Sec. 2 matters here: counting the wide pairs with $x \leq 1$ as escapes raises χ^2 to 47 and produces a spurious drift of α with age, because those configurations accumulate in time.

The binary produced by the escape is reproduced as well: its energy agrees within 0.05 and its median eccentricity within 0.025 in every angular-momentum bin, and at equal masses the eccentricity distribution is reproduced for every L. With the gate at $R = 10$ the agreement is good except at $L \approx 0$, where the theory lies about 2.5σ above the data ($\chi^2 = 13$, 9.6 and 4.1 for the three age cuts, improving with age). The prediction converges for $R \geq 10$ in three dimensions (Sec. 9); in the plane we report the $L \approx 0$, $R = 10$ excess as an open residual.

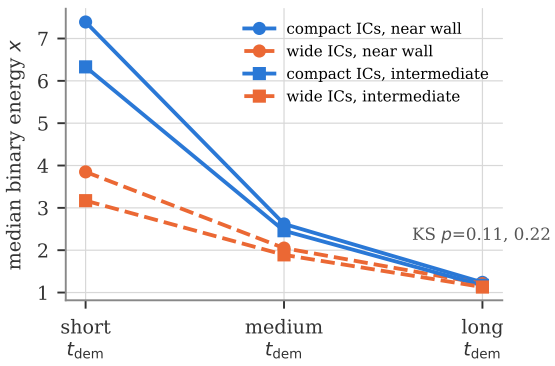

Figure 3: Median binary energy $x = E_B/E$ for compact and wide initial conditions, at two levels of closest approach, as a function of the duration of the democratic phase (terciles). Memory of the initial conditions is erased when the democratic phase is long.

Memory of initial conditions. Prompt escapes remember how the triple was set up. We drew initial conditions from a compact disk ($R_0 = 0.5$) and a wide one ($R_0 = 2.0$) and compared the binary energy at fixed closest approach $r_{\rm min}$ and fixed duration $t_{\rm dem}$ of the democratic phase (Fig. 3). At fixed $r_{\rm min}$ the two families remain different: proximity to collision does not carry the memory. At fixed $t_{\rm dem}$ the difference disappears once the democratic phase is long (Kolmogorov–Smirnov $p = 0.11$ and 0.22), whatever $r_{\rm min}$. The binary energy correlates with $t_{\rm dem}$ (Spearman -0.61) and hardly with $r_{\rm min}$ (-0.08). The democratic duration, which excludes the kinematic flight time of the escaper, is therefore the correct separator between prompt and relaxed escapes; the total lifetime is not, because the duration of the final excursion is a consequence of the binary energy (its correlation with x is -0.997).

Restricting to the quartile with the longest democratic phase, three different generators (compact, medium and wide disks) give $\alpha = 2.28\pm0.25$, 2.37 ± 0.19 and 2.08 ± 0.24, mutually consistent, with a weighted mean of 2.26 ± 0.13. The overall exponents of the three generators (1.60, 1.98, 2.60) differ because they contain different prompt populations; a value close to 2 for a single generator is therefore not by itself a confirmation of the relaxed theory. The difference between this value and the relaxed phase-space value 2 is 2σ; a sample about fifteen times larger is required to decide between them.

9 Three dimensions and comparison with Stone–Leigh

In three dimensions we integrated 18 000 orbits and evaluated the gate on 44 000 states. The binary is reproduced in every bin: median eccentricity within 0.03 and median energy within 0.03 (Table 3). The chaotic-past condition is essential in 3D: the unconditioned gate, which includes scattering states, does not reproduce the binary-energy distribution. The mass exponent of the simulations is $\alpha \approx 3.0$–3.5, close to the relaxed value 3. The gate prediction for α is consistent, but the test is weak: the heavy body escapes in only about 2% of cases, so its channel is poorly sampled and only two bins have useful errors (±0.27), where the deviation is below 1σ.

Stone–Leigh. We implemented Eq. (2) of Ref. [11] independently, with the strong-interaction radius $R = \alpha_R\, a_B(1+e_B)$, and integrated it on a deterministic grid. Before using it we checked it against the analytic limits given in that paper (Appendix A): at $L_0 \to 0$ the binary-energy tail has slope -3.51 against the published $-7/2$, and the eccentricity distribution converges to the published $e(1+e)/\sqrt{1-e^2}$ in the asymptotic regime in which that form is derived. For the masses 1:0.6:0.3 the formula gives $\alpha = 5.06$, 5.15, 5.12 and 5.31 in the first four bins of $L^2|E|$; changing α_R from 2 to 5 moves these values by less than 0.1. On a second, larger sample of 29 557 three-dimensional escapes (age ≥ 50) the simulations give $\alpha = 3.40$ [3.17, 3.72], 3.66 [3.45, 3.94], 3.15 [3.06, 3.28], 3.24 [3.15, 3.37] and 3.76 [3.51, 4.17] (95% intervals). The ergodic-volume theory thus overestimates the mass selectivity by about 1.5–2 in the exponent at unequal masses. It also does not follow the decrease of the binary eccentricity with angular momentum (0.82 against 0.67 in the fourth bin) and overestimates the binary energy (Fig. 4). We note one source of uncertainty: the radius parameter of Ref. [11] was not recalibrated for unequal masses, although its influence on α is small.

10 Where the entropy lives

We followed 17 847 planar orbits to $t = 10^4$ with exact tangent dynamics in the reduced space and split the time series into phases. Table 4 gives the time fraction and the mean entropy rate of each phase. Democratic phases take 4.6% of the time and carry $h_{\rm KS} = 0.311$ [0.298, 0.320]. Calm phases take 89.9% of the time with a mean rate of 0.0155, twenty times lower. The ratio between the two is stable under changes of the thresholds that define them: between 0.047 and 0.098 for every variant tested (democratic cut at 2.5, 3 or 4; calm cut at $4a$, $6a$ or $10a$; masses 1:1:1 and 1:0.3:0.1; no angular-momentum cut), and it decreases as the calm definition is made stricter.

The mean calm-phase entropy falls with the length of the calm phase (Fig. 5, right): 0.093, 0.058, 0.031, 0.014 and 0.0050 for orbits whose longest calm phase lasts 0–50, 50–200, 200–800, 800–3000 and 3000–10^4. Along individual long calm segments the accumulated tangent growth does not increase with duration (Fig. 5, left; 1 977 segments between 800 and 10^4): the median stays between 8 and 10 and the 90th percentile between 16 and 17 while the duration grows tenfold. The slope bounds the entropy rate of long calm segments to $h_{\rm KS} \lesssim 10^{-4}$, about 3000 times below the democratic rate; within the precision of the measurement $h_{\rm KS} = 0$. Checking the same segments in the full and in the reduced tangent space gives the same flat growth, so the

Table 3: Three-dimensional outcomes (masses 1:0.6:0.3, age ≥ 50, gate $R = 10$): mass exponent, median binary eccentricity and median binary energy x, simulations against gate theory.

$L^2\lvert E\rvert$	α sim / gate	e_B sim / gate	x sim / gate
0–0.03	3.51 ± 0.20 / 3.16 ± 1.37	0.826 / 0.836	1.21 / 1.23
0.03–0.06	3.28 ± 0.16 / –	0.745 / 0.775	1.20 / 1.23
0.06–0.12	3.19 ± 0.11 / 3.39 ± 0.27	0.693 / 0.681	1.14 / 1.14
0.12–0.25	2.99 ± 0.09 / 3.25 ± 0.26	0.667 / 0.646	1.10 / 1.11
0.25–0.50	3.85 ± 1.32 / –	0.600 / 0.606	1.06 / 1.07

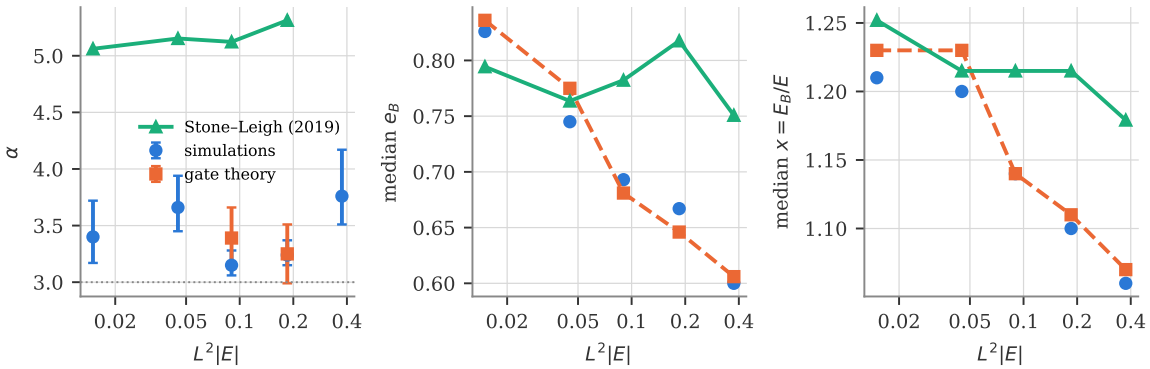

Figure 4: Three-dimensional outcomes against angular momentum. Left: mass exponent from 29 557 simulated escapes (circles, 95% intervals), gate theory in the two bins with useful statistics (squares) and our implementation of Stone and Leigh [11] (triangles); the dotted line is the relaxed value 3. Centre and right: median binary eccentricity and energy from the 18 000-orbit sample used for the gate comparison.

Table 4: Phase-resolved entropy rate (reduced space, 17 847 orbits to $t = 10^4$, masses 1:0.6:0.3). Brackets: 95% intervals.

phase	time fraction	h_{KS}
democratic	4.6%	0.311 [0.298, 0.320]
intermediate	3.8%	0.103 [0.090, 0.119]
calm	89.9%	0.0155 [0.0148, 0.0162]
unbound	1.7%	0.015

regularity is a property of the shape dynamics and not of the centre-of-mass or rotational directions.

Three families of calm phases. Classifying calm phases by the semi-major axis a_{out} of the outer orbit gives three families. *Compact* hierarchies (33% of calm time) are regular: the third body makes 10^2–10^3 revolutions around the pair while the tangent growth stays flat, a motion on a torus in which the binary's centre of mass acts as a stable pivot (a "fourth quasi-body"). *Far excursions* (39%) are regular trivially, because the third body is nearly decoupled. *Intermediate* hierarchies (27%) are weakly chaotic: their growth increases with duration with slope 1.6×10^{-3} $[1.1,\ 2.3]\times10^{-3}$, and in these systems the outer semi-major axis diffuses from 3–6 to 90–760 before escape. Late escapes come from this family.

Survivors. Of the systems still bound and regular at $t = 2 \times 10^5$, twelve were examined individually. Eight are on far excursions with outer periods of 2×10^5 to 2×10^6; their next pericentre passage, at 0.1–3.3 binary separations, will return them to chaos. Four are genuinely stable compact hierarchies with $a_{\mathrm{out}} = 2$–7; all four pass the Mardling–Aarseth criterion with a margin of 1.3–1.8, and all share the same structure: the two light bodies $(0.6 + 0.3)$ form the inner pair, the heavy body is outside, and the orbit is retrograde (109°–171°).

How calm phases end. In spontaneous calm phases the inner eccentricity oscillates by only 0.0025 [0.0023, 0.0027] (median), at any inclination: the phases last about 900 time units, while the Kozai period here is $\gtrsim 10^4$. No variable of the inner pair anticipates the end of a calm phase; 65% end directly in a democratic phase, and the end is abrupt. For the escaped systems, the end is the return of the third body to a pericentre of 0.7–3.6 binary separations. The lifetime distribution of escaped systems has a power-law tail with exponent 1.70 [1.63, 1.76] between 300 and 3000, and 1.67 [1.53, 1.81] between 3000 and 3×10^4; the durations of calm phases are distributed with exponent 2.00 [1.94, 2.05], consistent with Keplerian excursions near the escape threshold.

11 The regular domain and the Mardling–Aarseth boundary

Spontaneous calm phases are almost all below the hierarchical stability threshold: 98% of the 1 277 calm phases with $a_{\mathrm{out}} < 100$ have $Y < 1$, where $Y = R_{p,\mathrm{out}}/R_{\mathrm{MA}}$ is the outer pericentre divided by the

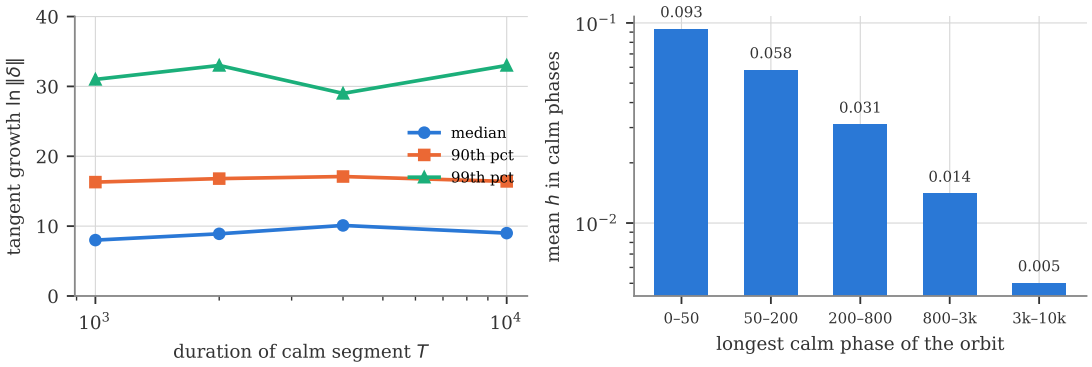

Figure 5: Entropy of calm phases. Left: accumulated tangent growth along continuous calm segments as a function of their duration (median, 90th and 99th percentiles); a chaotic segment with the democratic rate would grow linearly with slope 0.3. Right: mean entropy rate in calm phases, grouped by the longest calm phase of the orbit.

Mardling–Aarseth critical distance [19] (with its inclination correction), and their outer eccentricity has median 0.98. To locate the boundary we constructed 2 140 hierarchical triples at $E = -0.5$: circular inner pair, outer pericentre at $Y = 0.5$–2.5, outer eccentricity 0, 0.3, 0.6, inclination 0°, 90°, 180°, the heavy or the light body outside, twelve random phases per cell, each followed to $t = 5000$ with tangent dynamics.

The fraction of regular triples is shown in Fig. 6. For coplanar prograde orbits the transition is sharp and occurs between $Y = 0.85$ and 1.0 (e.g. from 27% to 100% regular): the Mardling–Aarseth threshold coincides with the boundary of $h_{\mathrm{KS}} = 0$ within 15%. Retrograde orbits are more stable than the formula predicts, with the boundary at $Y \approx 0.7$, consistent with the retrograde orientation of the four stable survivors. Polar orbits are less stable: Kozai–Lidov cycles drive the inner eccentricity to close encounters. With the light body outside the boundary moves to $Y \approx 1.3$; with the heavy body outside most polar triples remain chaotic up to $Y = 2.5$, with $h_{\mathrm{KS}} \approx 0.01$. Triples that break up have $h_{\mathrm{KS}} \approx 0.1$; triples that survive without being regular have $h_{\mathrm{KS}} \approx 0.01$–$0.025$.

Within this experiment, the set on which $h_{\mathrm{KS}} = 0$ is the hierarchical stability domain: the Mardling–Aarseth threshold, displaced inwards for retrograde orbits and outwards by Kozai–Lidov cycles for polar orbits. Outside it, a hierarchical phase is transient and ends in a democratic encounter. The limitation is the horizon of 5000 time units.

12 Discussion

What a statistical solution is. A solution of the kind given here is not an integrable solution: Poincaré's obstruction stands, and no orbit is predicted. What is predicted is the distribution of outcomes from the conserved quantities and the masses alone. For a chaotic problem this is the strongest form of prediction available, and it is the sense in which Stone and Leigh [11] and Kol [12] use the term.

Relation to previous theories. The gate measure belongs to the flux family of Kol, not to the volume family of Stone and Leigh: no strong-interaction radius is chosen, and the gate radius only needs to be large enough ($R \geq 10$ in 3D) for the result to converge. The difference with Kol is that the chaotic ingredient is computed by integrating each gate state backwards. This costs integrations but removes the need for a separate absorptivity measurement and makes unequal masses accessible. It also explains why a purely ergodic count fails at unequal masses: the states it counts include scattering states, whose past is not chaotic and whose channel populations differ. Large-scale measurements of the chaotic absorptivity and of its predictive power at equal masses were made by Manwadkar, Trani and Kol [14]; the gate provides an independent determination at unequal masses.

The ECR picture. The three parts of this work fit in one classification by h_{KS}. Regular islands ($\mathcal{M}_{\mathrm{ECR}}$) have $h_{\mathrm{KS}} = 0$ by Kolmogorov libration (Lagrange at dominant mass) or by a resonant modulation with non-degenerate lateral torsion (the stable choreographies). The transient has two unstable directions and $h_{\mathrm{KS}} = 0.067$ on average, but resolved in time its chaos is concentrated in democratic encounters ($h_{\mathrm{KS}} \approx 0.3$); compact hierarchies inside the inclination-corrected Mardling–Aarseth domain and far excursions are regular, and intermediate hierarchies are weakly chaotic and feed late escapes. The final state has $h_{\mathrm{KS}} = 0$. The statistical measure is conditioned on exactly the history that this classification identifies. "Chaos ends" is therefore not a universal law, but a property of open gravitational systems with an unbounded potential well (Sec. 5).

Limitations. The statistical and entropy results use one fourth-order scheme, checked by step halving but not against a regularised integrator. Most tests use one unequal-mass set and $E = -0.5$, with other energies related by exact scaling. The 3D gate prediction for α is limited by the sampling of the heavy-body channel. The regular-domain map extends to $t = 5000$. The

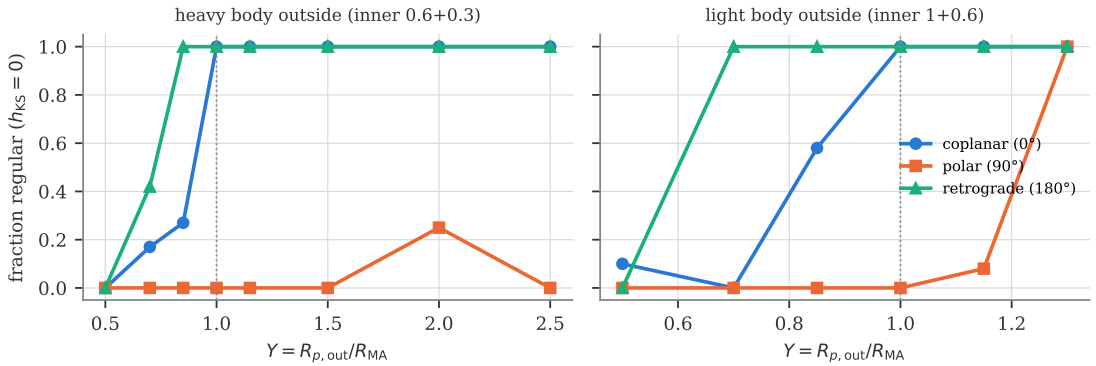

Figure 6: Fraction of constructed hierarchical triples that are regular ($h_{\rm KS} = 0$, tangent growth $\propto \ln T$) to $t = 5000$, against the outer pericentre in units of the Mardling–Aarseth critical distance, for circular outer orbits. Left: heavy body outside; right: light body outside. The dotted line marks $Y = 1$.

Mathieu reduction of the figure-eight compresses a 12×12 problem into two scalars and places the orbit close to a stability boundary. Apart from the sign of the lateral torsion determinant, none of the results is a theorem.

Open problems. (i) Whether the relaxed planar mass exponent is 2 or about 2.25. (ii) The origin of the $L \approx 0$ excess with the gate at $R = 10$ in the plane, and of a residual of 0.01–0.03 in the 3D eccentricity. (iii) An analytic expression for the fraction of gate states with chaotic past, which would make the theory predictive without backward integrations. (iv) The persistence probability $p \approx 0.37$ and the codimension excess of the basin boundary from lobe dynamics. (v) The Kantz–Grassberger relation with two unstable directions and partial dimensions. (vi) A Nekhoroshev-type estimate of stability times for the figure-eight; with the certified torsion sign the present estimates span 10^{17}–10^{53} periods and are only qualitative. (vii) A rigorous reduction of the figure-eight variational problem to the Mathieu form, with uncertainties on $(p, q_{\rm amp})$. (viii) The extension of the regular-domain map beyond $t = 5000$ and to other mass ratios.

13 Conclusions

Using the Kolmogorov–Sinai entropy rate as a classifier of dynamical states organises the three-body problem into regular islands, a chaotic transient and a final state. The figure-eight is stable because the gravitational gain along it is modulated at a frequency that falls in a narrow stable band of the corresponding Mathieu problem, while its lateral torsion is nondegenerate; the Lagrange configurations are stable by libration only at dominant mass. The transient lives on a saddle with two unstable directions, entered from the Lagrange region and left through binary hierarchy; it ends because the potential has no floor. Following Boltzmann rather than Poincaré, the outcome distribution is obtained by counting outgoing states with the Liouville measure at a sphere in Jacobi coordinates and keeping only those whose past is chaotic and whose future is an escape. The result has no free parameters, reproduces which body escapes and with what binary for unequal masses in two and three dimensions, and outperforms the ergodic-volume theory. Resolving $h_{\rm KS}$ in time locates the chaos in democratic encounters and identifies the regular hierarchical domain with the Mardling–Aarseth boundary modified by inclination and by Kozai–Lidov cycles.

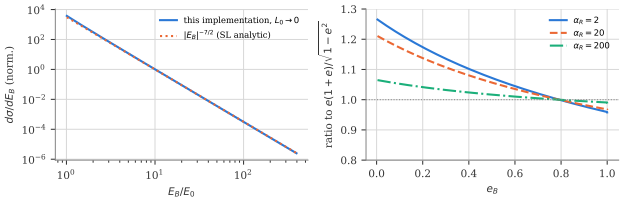

Figure 7: Checks of our implementation of Ref. [11] at $L_0 \to 0$, equal masses. Left: binary-energy distribution against the published $|E_B|^{-7/2}$. Right: eccentricity distribution relative to the published limit $e(1+e)/\sqrt{1-e^2}$, evaluated with the leading term of Eq. (2) for increasing α_R.

A Validation of the Stone–Leigh implementation

We evaluate Eq. (2) of Ref. [11] with $G = 1$ on a grid in $x = E_B/E_0 \in [1, 400]$ (logarithmic), $e_B = \sin\theta$ and $C_B = \hat{L}_B \cdot \hat{L}_0$, with $L_B = L_{\rm max}\sqrt{1-e_B^2}$ and $R = \alpha_R a_B(1+e_B)$. Fig. 7 shows two checks against the analytic limits stated in that paper for $L_0 \to 0$. The energy distribution has slope -3.51 (published $-7/2$). The eccentricity distribution approaches $e(1+e)/\sqrt{1-e^2}$ when the arccosh term of Eq. (2) is dropped and α_R is large, which is the regime in which that form is derived; with the full expression it differs by at most 16% at small e. The factor $(1+e_B)$ in the published limit is reproduced only with $R \propto a_B(1+e_B)$, which confirms the parametrisation. The same code at equal masses gives equal escape probabilities in the three channels, as it must.

Declarations

Funding. The author declares that no funds, grants, or other support were received during the preparation of this manuscript.

Competing interests. The author has no relevant financial or non-financial interests to disclose.

Author contributions. D.S. is the sole author. He conceived the study, designed and performed the numerical experiments and analysis, and wrote and reviewed the manuscript.

Data availability. The data generated and analysed during this study, the integrators (C), the gate code, the Stone–Leigh implementation and the analysis scripts (Python) are available from the corresponding author on reasonable request.

Use of AI tools. A large language model (Claude, Anthropic) was used to assist with code development, numerical analysis and the drafting of the text. The author designed the study, checked the results and takes full responsibility for the content.

References

[1] H. Poincaré, *Les Méthodes Nouvelles de la Mécanique Céleste* (Gauthier-Villars, Paris, 1892).

[2] K. F. Sundman, Acta Math. **36**, 105 (1912).

[3] T. A. Agekyan and Z. P. Anosova, Astron. Zh. **44**, 1261 (1967).

[4] E. M. Standish, Astron. Astrophys. **21**, 185 (1972).

[5] P. Hut and J. N. Bahcall, Astrophys. J. **268**, 319 (1983).

[6] J. J. Monaghan, Mon. Not. R. Astron. Soc. **176**, 63 (1976).

[7] J. J. Monaghan, Mon. Not. R. Astron. Soc. **177**, 583 (1976).

[8] P. E. Nash and J. J. Monaghan, Mon. Not. R. Astron. Soc. **184**, 119 (1978).

[9] M. Valtonen, A. Mylläri, V. Orlov and A. Rubinov, Mon. Not. R. Astron. Soc. **364**, 91 (2005).

[10] M. Valtonen and H. Karttunen, *The Three-Body Problem* (Cambridge University Press, Cambridge, 2006).

[11] N. C. Stone and N. W. C. Leigh, Nature **576**, 406 (2019).

[12] B. Kol, Celest. Mech. Dyn. Astron. **133**, 17 (2021).

[13] V. Manwadkar, B. Kol, A. A. Trani and N. W. C. Leigh, Mon. Not. R. Astron. Soc. **506**, 692 (2021).

[14] V. Manwadkar, A. A. Trani and B. Kol, Celest. Mech. Dyn. Astron. **136**, 4 (2024).

[15] Y. B. Ginat and H. B. Perets, Phys. Rev. X **11**, 031020 (2021).

[16] V. Manwadkar, A. A. Trani and N. W. C. Leigh, Mon. Not. R. Astron. Soc. **497**, 3694 (2020).

[17] G. Benettin, L. Galgani, A. Giorgilli and J.-M. Strelcyn, Meccanica **15**, 9 (1980).

[18] Ya. B. Pesin, Russ. Math. Surv. **32**(4), 55 (1977).

[19] R. A. Mardling and S. J. Aarseth, Mon. Not. R. Astron. Soc. **321**, 398 (2001).

[20] Y. Kozai, Astron. J. **67**, 591 (1962).

[21] M. L. Lidov, Planet. Space Sci. **9**, 719 (1962).

[22] E. J. Routh, Proc. London Math. Soc. **6**, 86 (1875).

[23] A. Deprit and A. Deprit-Bartholomé, Astron. J. **72**, 173 (1967).

[24] A. Chenciner and R. Montgomery, Ann. Math. **152**, 881 (2000).

[25] T. Kapela and C. Simó, Nonlinearity **20**, 1241 (2007).

[26] M. Šuvakov and V. Dmitrašinović, Phys. Rev. Lett. **110**, 114301 (2013).

[27] J. Moser, *Stable and Random Motions in Dynamical Systems* (Princeton University Press, Princeton, 1973).

[28] C. Simó, in *European Congress of Mathematics*, Progress in Mathematics Vol. 201 (Birkhäuser, Basel, 2001), p. 101.

[29] G. E. Roberts, Ergod. Theory Dyn. Syst. **27**, 1947 (2007).

[30] R. Montgomery, Nonlinearity **11**, 363 (1998).

[31] H. Kantz and P. Grassberger, Physica D **17**, 75 (1985).

[32] S. W. McDonald, C. Grebogi, E. Ott and J. A. Yorke, Physica D **17**, 125 (1985).

Supplementary Files

This is a list of supplementary files associated with this preprint. Click to download.

- ECRThreeBodyv2sources.zip